LETTER

doi:10.1038/nature18314

Photodissociation of ultracold diatomic strontium molecules with quantum state control

M. McDonald[1], B. H. McGuyer[1], F. Apfelbeck[1]†, C.-H. Lee[1], I. Majewska[2], R. Moszynski[2] & T. Zelevinsky[1]

Chemical reactions at ultracold temperatures are expected to be dominated by quantum mechanical effects. Although progress towards ultracold chemistry has been made through atomic photoassociation[1], Feshbach resonances[2] and bimolecular collisions[3], these approaches have been limited by imperfect quantum state selectivity. In particular, attaining complete control of the ground or excited continuum quantum states has remained a challenge. Here we achieve this control using photodissociation, an approach that encodes a wealth of information in the angular distribution of outgoing fragments. By photodissociating ultracold $^{88}Sr_2$ molecules with full control of the low-energy continuum, we access the quantum regime of ultracold chemistry, observing resonant and nonresonant barrier tunnelling, matter–wave interference of reaction products and forbidden reaction pathways. Our results illustrate the failure of the traditional quasiclassical model of photodissociation[4–7] and instead are accurately described by a quantum mechanical model[8,9]. The experimental ability to produce well-defined quantum continuum states at low energies will enable high-precision studies of long-range molecular potentials for which accurate quantum chemistry models are unavailable, and may serve as a source of entangled states and coherent matter waves for a wide range of experiments in quantum optics[10,11].

To obtain full control over the initial (molecular) and final (continuum) quantum states, we photodissociate diatomic strontium molecules ($^{88}Sr_2$) that are optically trapped at a temperature of ~5 μK (ref. 12). These molecules are produced by photoassociating laser-cooled Sr atoms in a far-off-resonant one-dimensional (1D) optical lattice with a depth of up to 50 μK. The Sr atoms are divalent and do not form covalent chemical bonds. However, the ground-state Sr_2 dissociation energy is larger than in typical van der Waals complexes and similar to hydrogen bonded systems such as the water dimer. The $^{88}Sr_2$ molecules that we produce are either weakly bound near the ground state threshold ($^1S + {}^1S$ atomic limit) or, with an extra step of optical preparation, near the lowest singly excited threshold ($^1S + {}^3P_1$). The long-lived (22 μs) excited atomic state $^3P_1$ is responsible for the low laser-cooling temperature, efficient molecule creation, accurate state preparation and high spectroscopic resolution that allows photodissociation very close to the threshold. Photodissociation is driven by a 10–20 μs pulse of linearly polarized 689 nm light (intensity 0.3–30 W cm^{-2}, bandwidth <200 Hz) propagating along the lattice axis. The light frequency is chosen to probe a continuum energy in the range of 0–15 mK because this matches typical electronic and rotational barrier heights. After a controlled delay, the fragments are detected by absorption imaging via the strong $^1S - {}^1P_1$ Sr transition using 461 nm light propagating almost parallel to the lattice axis, so that the initial sample of $>10^4$ molecules appears as a point source. This produces a 2D projection of the 3D spherical shell (Newton sphere) formed by the expanding fragments. The experimental geometry is illustrated in Fig. 1, including the definition of angles θ and ϕ for a dissociating molecule and an image of the fragments showing clear dependence on both angles. The arrangement of the optical lattice, the photodissociating and imaging light, a camera and a small bias magnetic field B that fixes the quantum axis are also shown. In all subsequent images the colour scheme is identical to that of Fig. 1b apart from the overall normalization and the fields of view are 0.1–0.9 mm on each side.

Following photodissociation, the angular distribution of fragment positions is described by an intensity (or differential cross-section)

$$I(\theta,\phi) = |f(\theta,\phi)|^2 \quad (1)$$

which is the square of a scattering amplitude f that can be expanded in terms of partial amplitudes, $f(\theta,\phi) = \sum_{JM} f_{JM}\psi_{JM}(\theta,\phi)$. This expansion uses angular basis functions ψ_{JM} of the outgoing electronic

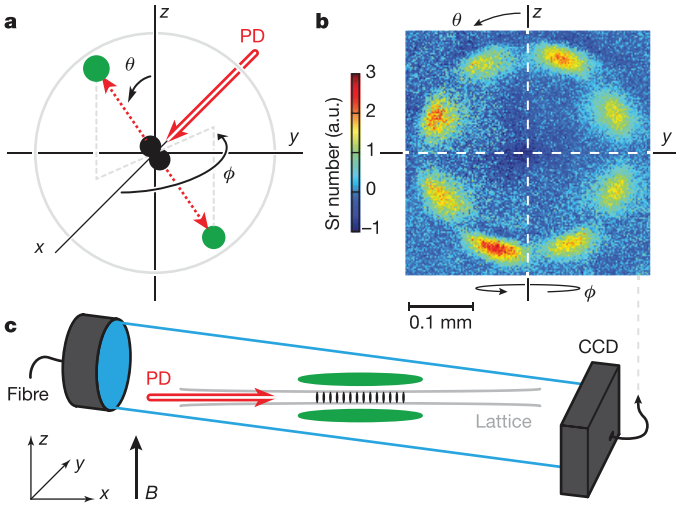

Figure 1 | Photodissociation of diatomic molecules in an optical lattice. **a**, A homonuclear molecule (black circles) producing fragments (green circles) with well-controlled speeds forms a Newton sphere. The distribution of the fragments on the sphere surface is parameterized by a polar angle θ relative to the z axis and an azimuthal angle ϕ relative to the x axis in the xy plane. The photodissociating (PD) light propagates along $+x$. **b**, An experimental image of the fragments corresponds to the Newton sphere projected onto the yz plane. This particular image is one of many we observed that is highly quantum mechanical in nature and distinctly lacks fragments that are emitted along the xz plane. The distribution is thus not cylindrically symmetric about the z axis and depends on ϕ in addition to θ. a.u., arbitrary units. **c**, The fragments (green ovals) are detected by absorption imaging using a charge-coupled device (CCD) camera and a wide light beam from an optical fibre. The photodissociating light is coaligned with the lattice axis along x. The imaging light is nearly coaligned with x (a small tilt is present for technical reasons). A magnetic field can be applied along the z axis.

[1]Department of Physics, Columbia University, 538 West 120th Street, New York, New York 10027-5255, USA. [2]Quantum Chemistry Laboratory, Department of Chemistry, University of Warsaw, Pasteura 1, 02-093 Warsaw, Poland. †Present address: Faculty of Physics, Ludwig Maximilian University of Munich, Schellingstrasse 4, 80799 Munich, Germany.

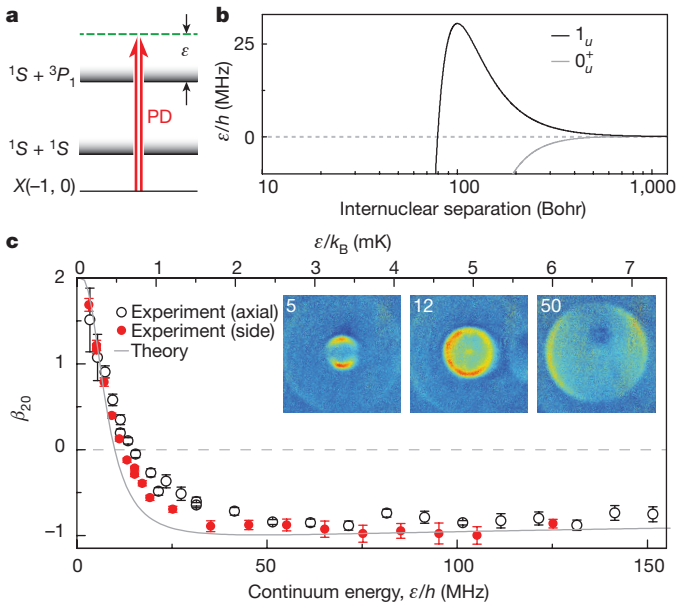

Figure 2 | Photodissociation to a multichannel continuum. a, Schematic for PD of $^{88}Sr_2$ in the initial ground state $X(v_i, J_i)$ to an excited continuum energy ε, which is subsequently expressed in MHz or in mK (via the Boltzmann constant k_B). **b**, Potential energy structure ($\lesssim$1 mK) of the $^1S + {}^3P_1$ continuum, showing both of the electronic potentials (0_u^+ and 1_u) that couple to the ground state via E1 transitions[9]. **c**, The angular anisotropy parameter β_{20} for this process measured by two imaging methods (using axial-view and side-view CCD cameras) and calculated using a quantum chemistry model. The inset images show fragments at three different energies ε/h labelled in MHz. The images and curves indicate a steep change in the angular anisotropy in the 0–2 mK continuum energy range. The experimental errors for axial imaging were estimated by varying the choice of centre point for the pBasex algorithm and averaging the results, and for side imaging from least-squares fitting to equation (2) convolved with a blurring function to account for experimental imperfections.

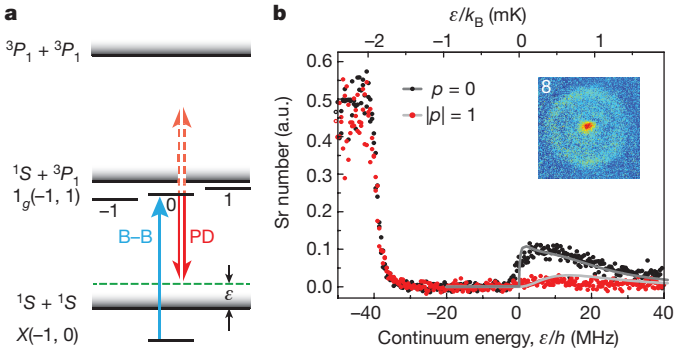

Figure 3 | E1-forbidden photodissociation experiment and theory. a, Molecules in $M_i = 0$ of the long-lived 1_g state below the $^1S + {}^3P_1$ threshold are prepared with a bound–bound (B–B) π pulse and fragmented at the gerade ground continuum with PD light. **b**, M1/E2 photodissociation produces photofragments for $\varepsilon > 0$ (right), and as predicted is strongest for $p = 0$. Solid curves are calculations of the total transition strength using a quantum chemistry model. E1 photodissociation to the $^3P_1 + {}^3P_1$ continuum also appears for $\varepsilon < 0$ (left). The inset image shows fragments for $p = 0$ and $\varepsilon/h \approx 8$ MHz. The strong central dot results from spontaneous E1-forbidden photodissociation of the molecules into low-energy atoms that are captured by the lattice.

channel, where J and M are the total angular momentum and its projection onto the quantum axis, respectively. The intensities for separate electronic channels superpose to produce the total intensity $I(\theta, \phi)$. Cylindrically asymmetric distributions with ϕ dependence are possible if several M states are coherently created because $\psi_{JM}(\theta, \phi) \equiv e^{iM\phi}\psi_{JM}(\theta, 0)$. Our measured angular distributions can be summarized with the parameterization

$$I(\theta, \phi) \propto 1 + \sum_{l=1}^{\infty} \sum_{m=0}^{l} \beta_{lm} \cos(m\phi) P_l^m(\cos\theta) \qquad (2)$$

where $P_l^m(\cos\theta)$ is an associated Legendre polynomial and l is restricted to even values for homonuclear diatomic molecules. The β_{lm} coefficients are directly related to the amplitudes f_{JM}, but hide some of the simplicity that is apparent from using the amplitudes with equation (1). Besides their use in photodissociation, fragment angular distributions are powerful observables in photoionization experiments[13] as they provide a route to completely measure the ionization matrix element amplitudes and phases[14]. The internal angular momenta of the fragments may also carry valuable information[15].

To investigate a multichannel electronic continuum at very low dissociation energies, ε, we prepared ultracold molecules in the $J_i = 0$ initial state of the least-bound vibrational level $v_i = -1$ (negative v_i count down from threshold) of the ground potential X and photodissociated them at the excited $^1S + {}^3P_1$ continuum via the electric dipole (E1) process illustrated in Fig. 2a with an applied field $B = 0$. There are four allowed channels in the excited continuum, which are labelled 0_u^+, 1_u, 0_g^+ and 1_g, where the letters u/g refer to the inversion symmetry of the wave function and the numbers 0/1 refer to the internuclear axis projection of the electronic angular momentum. Only u-symmetric channels are E1-accessible from the ground state. Here, the light polarization sets the quantum axis along z and the fragments can only have $J = 1$, $M = 0$ quantum numbers because $J \geq 1$ for the 0_u^+ and 1_u electronic potentials shown in Fig. 2b. As 1_u has an $\sim$30 MHz ($\sim$1.5 mK) repulsive electronic barrier, we expect the fragment angular distribution to evolve in the probed energy range due to barrier tunnelling. We observe a steep variation of the single anisotropy parameter needed to describe this process, β_{20} from equation (2). Two methods were used to measure this data: axial-view imaging processed with the pBasex algorithm[16] and side-view imaging integrated along the lattice and fitted to a density profile. Figure 2c shows that both methods agree and reveals an evolution of the fragment distribution from a parallel dipole ($\beta_{20} \approx 2$ at $\varepsilon/h \approx 5$ MHz where h is Planck's constant) to a uniform shell ($\beta_{20} \approx 0$ at $\varepsilon/h \approx 12$ MHz) and then a perpendicular dipole ($\beta_{20} \approx -1$ at $\varepsilon/h \approx 50$ MHz). A quantum chemistry model[8,9] was used to calculate the expected anisotropy curve in Fig. 2c by connecting the bound and continuum wave functions via Fermi's golden rule to compute the amplitudes f_{JM}, showing strong qualitative agreement with the data. The theoretical 0_u^+ and 1_u Coriolis-mixed potentials agree well with high-precision bound-state $^{88}Sr_2$ spectroscopy[9,17], but this work is the first test of their predictive power in the continuum.

E1-forbidden photodissociation is an important effect in atmospheric physics and must be considered when calculating the total absorption cross section for molecular oxygen within the so-called Herzberg continuum. Surprisingly, however, neither magnetic dipole (M1) nor electric quadrupole (E2) photodissociation has been directly observed previously. In most cases E1 is also present, making it challenging to study the weaker M1/E2 processes. However, experiments with ultracold Sr_2 allow measurements of pure M1/E2 photodissociation and a comparison with quantum mechanical calculations. Using resonant π pulses we prepare metastable molecules in a $J_i = 1$, $M_i = 0$ state of the least-bound vibrational level of the subradiant 1_g potential that has no E1 coupling to the ground state[12], as sketched in Fig. 3a. The frequency of the dissociating light was varied as shown in Fig. 3b. Here $p = 0$ ($|p| = 1$) implies that the light polarization has a magnetic field parallel (perpendicular) to the quantum axis. The prominent, polarization-independent feature on the left ($\varepsilon < 0$) is E1 photodissociation above the $^3P_1 + {}^3P_1$ threshold, whereas the weaker, polarization-dependent feature on the right is M1/E2 photodissociation. As the figure shows, the strength of this

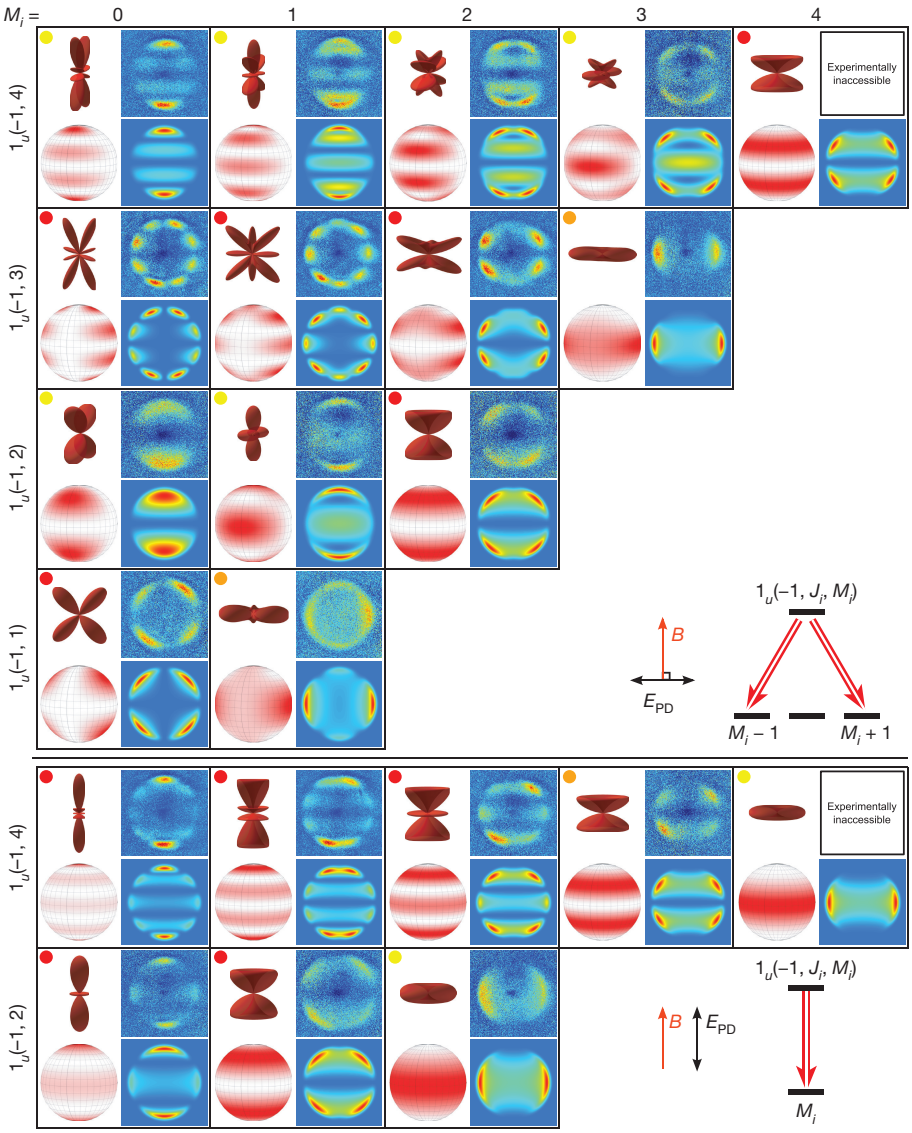

Figure 4 | Photodissociation of singly excited ($^1S + {}^3P_1$) molecules to the ground-state continuum with energies of several millikelvin. Each row and column corresponds to molecules prepared in the indicated $1_u(v_i, J_i)$ state and M_i sublevel. ($M_i = 4$ was not accessible experimentally.) The upper and lower sections correspond to PD light polarizations $|p| = 1$ and 0, respectively, where the PD laser's electric field is E_{PD}. Within each square panel, the experimental image is on the top right, with a comparable simulation of a projected Newton sphere on the bottom right. The full sphere rendition is on the bottom left and the top left shows the mapping of the fragment detection probability at each angle onto the radial coordinate of a surface. For $|p| = 1$, matter–wave interference occurs if two values of M are produced, leading to strongly ϕ-dependent patterns. For each case, the degree of agreement with the quasiclassical approximation is indicated by a coloured dot, as explained in the text.

forbidden process tapers off rapidly and is substantial only below ~1 mK. The inset displays fragments near the peak of the $p = 0$ spectrum. Although the number of fragments for $p = 0$ is unaffected by interference between M1 and E2 pathways, our calculations indicate that their angular distributions (Extended Data Fig. 1) are sensitive to this rarely observed interference.

We take advantage of the single-channel spinless ground state of $^{88}Sr_2$ to explore chemistry in the ultracold regime, obtain a library of fragment distributions and test a quasiclassical model of photodissociation. We prepare singly excited ($^1S + {}^3P_1$) molecules with quantum numbers J_i, M_i and immediately photodissociate them at the $^1S + {}^1S$ ground state continuum, in some cases applying B up to 20 G to enable symmetry-forbidden E1 transitions[18]. To control the final value of J in the continuum (which quantum statistics requires to be even for bosonic ground-state $^{88}Sr_2$) we either obtain a unique J by choosing to start from an even J_i and taking advantage of selection rules, or, if multiple 'partial waves' with different J are possible and interfere, we choose an ε value at which a single J wave strongly dominates, as discussed below. To control the final values of M we orient the linear polarization of the photodissociating light either parallel ($p = 0$) to the quantum axis, for which selection rules ensure $M = M_i$, or perpendicular ($|p| = 1$), for which $M = M_i \pm 1$. Thus, we are able to engineer and image different continua in either pure M states or as their coherent quantum interference. Disruption from Zeeman shifts is avoided because the ground continuum is practically nonmagnetic.

Figure 4 shows a full range of distributions parameterized by equation (1) with either $f(\theta, \phi) = Y_{J,M_i}(\theta, \phi)$ or $f(\theta, \phi) = \sqrt{R}\, Y_{J,M_i-1}(\theta, \phi) + e^{i\delta}\sqrt{1-R}\, Y_{J,M_i+1}(\theta, \phi)$. Here the spherical harmonics $Y_{JM} = \Psi_{JM}$ for the ground continuum, R and δ are the relative amplitude and phase parameters and $J = 2$ or 4. (At the chosen continuum energies, the $p = 0$ patterns for $J_i = 1, 3$ would be nearly redundant with $J_i = 2, 4$ and so are omitted.) Quantum mechanical calculations, included for comparison, assume that the continuum states are dominated by the higher J contribution. Figure 4 suggests the following observations. First, the coherent superposition of a pair of M, which occurs for $|p| = 1$ but not $p = 0$, leads to clean observations of distributions without

cylindrical symmetry, previously unreported for diatomic molecules. In particular, multiple cases are shown of a molecule fragmenting into up to eight distinct (θ, ϕ) regions. Second, the same final states ($J=4$, $M=\pm1$) are produced for $|p|=1$, $M_i=0$ and $J_i=4$, 3 at the chosen continuum energies. Thus we could expect to observe identical fragment patterns. However, a subtle point is that odd J_i and even J_i produce $M=M_i\pm1$ probability amplitudes with an opposite relative phase. This results in identical ϕ-dependent patterns rotated by 90° relative to each other. The same mapping of the relative phase onto the rotation angle occurs for $|p|=1$, $M_i=0$ and $J_i=2$, 1. Third, the previous point roughly holds for the higher values of M_i as well, but non-identical populations of $M=M_i\pm1$ are produced due to asymmetrical coupling strengths. For example, the matter–wave interference patterns for $(J_i, M_i)=(4, 2)$ and $(3, 2)$ are not only rotated relative to each other, but have slightly different shapes.

Over the past few decades a quasiclassical model has been advanced to predict the angular distributions for single-photon E1 photodissociation of diatomic molecules prepared in arbitrary quantum states[6,7,19]. This approach multiplies the conventional distribution[4,5] for molecules prepared in spherically symmetric states or ensembles, $I(\theta)\propto 1+\beta_{20}P_2^0(\cos\chi)$, by a probability density $|\Phi_i|^2$ for the initial molecular axis orientation, which gives $I(\theta,\phi)\propto|\Phi_i(\theta,\phi)|^2[1+\beta_{20}P_2^0(\cos\chi)]$ where $\chi=(\theta,\phi)$ is the polar angle defined with respect to the orientation of linear polarization of the photodissociating light and (θ,ϕ) are defined by the quantization axis, as before. This intuitive model suggests that photodissociation probes the 'shape' of the initial molecules, as detailed in Extended Data Fig. 2. Its validity, however, has been questioned over the years[20].

To indicate the level of agreement with the quasiclassical model, we include coloured dots for each pattern in Fig. 4. A green dot indicates exact agreement between the quasiclassical and quantum mechanical calculations, a yellow dot indicates qualitative agreement that cannot be made exact by adjusting β_{20}, an orange dot indicates disagreement that can become a qualitative agreement by adjusting β_{20} and a red dot indicates clear disagreement for all β_{20}—usually because fragments are observed where $|\Phi_i|^2$ has a node. For all cases in Fig. 4 the quasiclassical model fails to varying degrees. Although this could be expected for the 1_u initial states[19], surprisingly even photodissociation of the 0_u^+ states (Extended Data Fig. 3) disagrees with the quasiclassical model in all cases where more than a single J is possible in the continuum. This is because only the single-J cases allow the quasiclassical assumption of prompt axial recoil to be satisfied at such low continuum energies. Furthermore, our experiments demonstrate that initial molecules with different shapes (for example, 0_u^+ versus 1_u) can produce nearly identical distributions, highlighting that the fragment distributions are solely determined by the final (continuum) states.

Ultracold photodissociation readily reveals features of the continuum just above the threshold. The ability to freely explore a large range of continuum energies, together with strict optical selection rules and cleanly prepared quantum states, provides a versatile tool to isolate and study individual reaction channels. Whereas Fig. 2 explored tunnelling through an electronic barrier, Fig. 5 shows the case when only rotational barriers are present. Here molecules prepared in the $0_u^+(v=-3, J_i=3, M_i=0)$ state are photodissociated with $p=0$, resulting in continuum states with $M=0$ and $J=2$, 4. This mixture can be described by equation (1) with $f(\theta,\phi)=\sqrt{R}\,Y_{20}(\theta,\phi)+e^{i\delta}\sqrt{1-R}\,Y_{40}(\theta,\phi)$. Figure 5a is a plot of the branching ratio R and the interference amplitude $2\cos\delta\sqrt{R(1-R)}$ for the 0–15 mK range of continuum energies. The data show a good qualitative agreement with quantum chemistry calculations, and reveal a predicted but so far unobserved g-wave shape resonance (or quasi-bound state) confined by the $J=4$ centrifugal barrier. This long-lived (~10 ns) resonance ~66 MHz above threshold could be used to control light-assisted molecule formation rates[21]. Shape resonances can also be mapped with magnetic Feshbach dissociation of ground-state molecules[22–24]. However, photodissociation is more widely applicable to molecules with any type of spin structure in any electronic state, and allows more control over the quantum numbers. In Fig. 5b an anisotropic, energy-independent pattern is visible on all images with a radius close to that of the 62 MHz image. We have confirmed that this signal arises from spontaneous photodissociation of the molecules into the g-wave shape resonance (Extended Data Fig. 4).

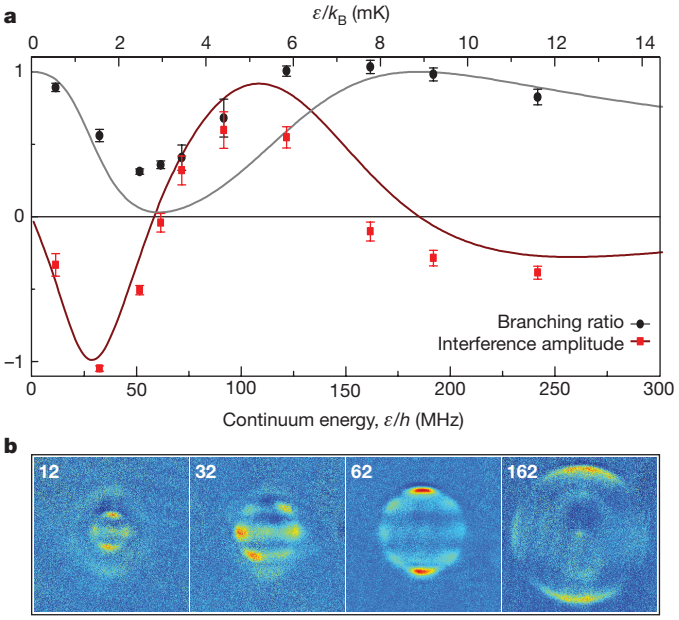

Figure 5 | Energy-dependent photodissociation near a shape resonance. **a**, Molecules prepared in the $0_u^+(v_i=-3, J_i=3, M_i=0)$ state are photodissociated at the ground continuum. For $p=0$, selection rules lead to a single $M=0$ but a mixture of $J=2$, 4. The branching ratio and interference amplitude of this mixture, as described in the text, evolve with energy and reveal a $J=4$ (g-wave) shape resonance at ~3 mK. The experimental data were analysed with pBasex and errors were estimated by varying the effective saturation intensity, used to process the absorption images, within its uncertainty. The theoretical curves were calculated with a quantum chemistry model. **b**, Images of fragments labelled by their continuum energies ε/h in MHz that show the evolution with energy. The faint anisotropic, energy-independent pattern with roughly the same radius as the 62 MHz image is from spontaneous decay into the shape resonance.

This work explores light-induced molecular fragmentation in the fully quantum regime. Quasiclassical descriptions are not applicable and our observations are dominated by coherent superpositions of matter waves originating from monoenergetic continuum states with different quantum numbers. The results agree with a state-of-the-art quantum chemistry model[8,9], but challenge the theory to describe more complicated phenomena. For example, preliminary observations of photodissociation to the doubly excited continuum (as in Fig. 3b) indicate rich structure near the threshold. This continuum is not well understood, while interactions near the $^3P_1+{}^3P_1$ threshold play a key role in recent proposals and experiments in ultracold many-body science[25]. Other excited continua with even longer lifetimes (for example, the subradiant 1_g and 0_g^+ manifolds) exist for Sr_2 and similar molecules and should enable the exploration of entangled continuum states. Photodissociation can shed light on the ultracold chemistry of a rich array of molecular states, as well as on new reaction mechanisms—as was shown here with M1/E2 photodissociation. With improved control of the imaging and of the optical lattice effects, experiments can get even closer to the threshold. We expect to reach nanokelvin fragment energies in the lattice, leading to high-precision measurements of binding energies for tests of fundamental physics and molecular quantum electrodynamics[26,27]. Ultralow fragment energies can also aid in the creation of novel ultracold atomic gases[28]. A promising future direction would be to enhance the quantum control achieved

here by manipulating the final continuum states with external fields[29,30]. We have shown the extreme sensitivity of weakly bound molecules to small magnetic fields[18], and the same principle applies just above threshold. This external control over ultracold chemistry should allow the study and manipulation of new reaction pathways.

Online Content Methods, along with any additional Extended Data display items and Source Data, are available in the online version of the paper; references unique to these sections appear only in the online paper.

Received 4 January; accepted 26 April 2016.

1. Jones, K. M., Tiesinga, E., Lett, P. D. & Julienne, P. S. Ultracold photoassociation spectroscopy: long-range molecules and atomic scattering. *Rev. Mod. Phys.* **78,** 483–535 (2006).
2. Chin, C., Grimm, R., Julienne, P. & Tiesinga, E. Feshbach resonances in ultracold gases. *Rev. Mod. Phys.* **82,** 1225–1286 (2010).
3. Ospelkaus, S. *et al.* Quantum-state controlled chemical reactions of ultracold potassium-rubidium molecules. *Science* **327,** 853–857 (2010).
4. Zare, R. N. & Herschbach, D. R. Doppler line shape of atomic fluorescence excited by molecular photodissociation. *Proc. IEEE* **51,** 173–182 (1963).
5. Zare, R. N. Photoejection dynamics. *Mol. Photochem.* **4,** 1–37 (1972).
6. Choi, S. E. & Bernstein, R. B. Theory of oriented symmetric-top molecule beams: precession, degree of orientation, and photofragmentation of rotationally state-selected molecules. *J. Chem. Phys.* **85,** 150–161 (1986).
7. Zare, R. N. Photofragment angular distributions from oriented symmetric-top precursor molecules. *Chem. Phys. Lett.* **156,** 1–6 (1989).
8. Skomorowski, W., Pawłowski, F., Koch, C. P. & Moszynski, R. Rovibrational dynamics of the strontium molecule in the $A\,^1\Sigma_u^+$, c $^3\Pi_u$, and $a\,^3\Sigma_u^+$ manifold from state-of-the-art ab initio calculations. *J. Chem. Phys.* **136,** 194306 (2012).
9. Borkowski, M. *et al.* Mass scaling and nonadiabatic effects in photoassociation spectroscopy of ultracold strontium atoms. *Phys. Rev. A* **90,** 032713 (2014).
10. Grangier, P., Aspect, A. & Vigue, J. Quantum interference effect for two atoms radiating a single photon. *Phys. Rev. Lett.* **54,** 418–421 (1985).
11. Kheruntsyan, K. V., Olsen, M. K. & Drummond, P. D. Einstein–Podolsky–Rosen correlations via dissociation of a molecular Bose–Einstein condensate. *Phys. Rev. Lett.* **95,** 150405 (2005).
12. McGuyer, B. H. *et al.* Precise study of asymptotic physics with subradiant ultracold molecules. *Nature Phys.* **11,** 32–36 (2015).
13. Reid, K. L. Photoelectron angular distributions. *Annu. Rev. Phys. Chem.* **54,** 397–424 (2003).
14. Hockett, P., Wollenhaupt, M., Lux, C. & Baumert, T. Complete photoionization experiments via ultrafast coherent control with polarization multiplexing. *Phys. Rev. Lett.* **112,** 223001 (2014).
15. Rakitzis, T. P., Kandel, S. A., Alexander, A. J., Kim, Z. H. & Zare, R. N. Photofragment helicity caused by matter–wave interference from multiple dissociative states. *Science* **281,** 1346–1349 (1998).
16. Garcia, G. A., Nahon, L. & Powis, I. Two-dimensional charged particle image inversion using a polar basis function expansion. *Rev. Sci. Instrum.* **75,** 4989–4996 (2004).
17. McGuyer, B. H. *et al.* High-precision spectroscopy of ultracold molecules in an optical lattice. *New J. Phys.* **17,** 055004 (2015).
18. McGuyer, B. H. *et al.* Control of optical transitions with magnetic fields in weakly bound molecules. *Phys. Rev. Lett.* **115,** 053001 (2015).
19. Beswick, J. A. & Zare, R. N. On the quantum and quasiclassical angular distributions of photofragments. *J. Chem. Phys.* **129,** 164315 (2008).
20. Seideman, T. The analysis of magnetic-state-selected angular distributions: a quantum mechanical form and an asymptotic approximation. *Chem. Phys. Lett.* **253,** 279–285 (1996).
21. González-Férez, R. & Koch, C. P. Enhancing photoassociation rates by nonresonant-light control of shape resonances. *Phys. Rev. A* **86,** 063420 (2012).
22. Volz, T. *et al.* Feshbach spectroscopy of a shape resonance. *Phys. Rev. A* **72,** 010704(R) (2005).
23. Mark, M. *et al.* Stückelberg interferometry with ultracold molecules. *Phys. Rev. Lett.* **99,** 113201 (2007).
24. Knoop, S. *et al.* Metastable Feshbach molecules in high rotational states. *Phys. Rev. Lett.* **100,** 083002 (2008).
25. Zhang, X. *et al.* Spectroscopic observation of SU(*N*)-symmetric interactions in Sr orbital magnetism. *Science* **345,** 1467–1473 (2014).
26. Bartenstein, M. *et al.* Precise determination of ^{6}Li cold collision parameters by radio-frequency spectroscopy on weakly bound molecules. *Phys. Rev. Lett.* **94,** 103201 (2005).
27. Salumbides, E. J. *et al.* Bounds on fifth forces from precision measurements on molecules. *Phys. Rev. D* **87,** 112008 (2013).
28. Lane, I. C. Production of ultracold hydrogen and deuterium via Doppler-cooled Feshbach molecules. *Phys. Rev. A* **92,** 022511 (2015).
29. Lemeshko, M., Krems, R. V., Doyle, J. M. & Kais, S. Manipulation of molecules with electromagnetic fields. *Mol. Phys.* **111,** 1648–1682 (2013).
30. Stapelfeldt, H. & Seideman, T. Colloquium: Aligning molecules with strong laser pulses. *Rev. Mod. Phys.* **75,** 543–557 (2003).

Supplementary Information is available in the online version of the paper.

Acknowledgements We gratefully acknowledge ONR grant N000-14-14-1-0802, NIST award 60NANB13D163, and NSF grant PHY-1349725 for partial support of this work, and thank A. T. Grier, G. Z. Iwata and M. G. Tarallo for discussions. R.M. acknowledges the Foundation for Polish Science for support through the MISTRZ programme.

Author Contributions M.M., B.H.M., F.A., C.-H.L. and T.Z. designed the experiments, carried out the measurements and interpreted the data. I.M. and R.M. carried out the calculations and interpreted the data. All authors contributed to the manuscript.

Author Information Reprints and permissions information is available at www.nature.com/reprints. The authors declare no competing financial interests. Readers are welcome to comment on the online version of the paper. Correspondence and requests for materials should be addressed to T.Z. (tz@phys.columbia.edu).

Reviewer Information *Nature* thanks D. Chandler and the other anonymous reviewer(s) for their contribution to the peer review of this work.

METHODS

Experimental details. After laser cooling a gas of atomic Sr in a 1D optical lattice, molecules were created via photoassociation to the $0_u^+(v=-4, J=1)$ excited state (binding energy 1,084 MHz) followed by well-directed spontaneous emission to the $X^1\Sigma_g^+(v=-1)$ ground states with $J=0$ or 2 (binding energies of 137 and 67 MHz, respectively)[17,31]. Any remaining atoms were removed with a pulse of imaging light. The molecular sample trapped in the lattice is about 20 μm in diameter and 200 μm long. To prepare metastable $1_g(v_i=-1, J_i=1)$ excited states (binding energy 19 MHz, lifetime ~5 ms), we used a lattice wavelength of ~910 nm to enable resonant 689 nm π pulses to transfer the population from $X(v=-1, J=0)$ to this state before photodissociation[12]. For our experimental conditions, this transfer was ~40% efficient. To prepare shorter-lived 0_u^+ or 1_u excited states, we used a 689 nm light pulse to drive a resonant bound–bound transition from either the $J=0$ or 2 ground state to the desired state during photodissociation. In both cases, we used the polarization of this light and excited-state Zeeman shifts[12,18,32] to select M_i. For reference, the binding energies for the $1_u(v_i=-1, J_i)$ excited states are 353 MHz for $J'=1$; 287 MHz for $J'=2$; 171 MHz for $J'=3$ and 56 MHz for $J'=4$; for the $0_u^+(v_i=-3, J_i=3)$ state, the binding energy is 132 MHz and for $0_u^+(-4,1)$ it is 1,084 MHz. The $^1S+{}^1S$ and $^1S+{}^3P_1$ thresholds may be spectroscopically located with kilohertz precision using the lineshape model of ref. 17.

The photodissociating light propagates along the tight-confinement x axis of the optical lattice (Gaussian waist ~40 μm), and is linearly polarized along either the y axis or the z axis. Except for Fig. 2, for which the net magnetic field is nearly zero, a field of a few to a few tens of gauss is applied along the z axis to fix a quantization axis for excited bound states. The ground bound and continuum states are insensitive to this field, so to avoid mixed-quantization effects from tensor light shifts[18] the optical lattice was linearly polarized along the z axis. We confirmed that our results are unaffected by the small lattice trap depth (typically 0.6–0.8 MHz). A full description of the laboratory-frame spherical tensor components of the fields driving the photodissociation transitions is available in the Supplementary Information.

After the photodissociating light pulse, the fragments were allowed to expand kinetically for several hundred microseconds before their positions were recorded with standard absorption imaging[33]. This expansion time is needed to mitigate blurring due to the finite pulse width and limited imaging resolution, but has the cost of diluting the signal over a larger area, which makes imaging artefacts more problematic. Therefore, we adjusted this expansion time as needed to optimize the signal-to-noise ratio and angular resolution.

Most absorption images were taken with imaging light aligned nearly along the x axis, projecting the fragment positions into the yz plane. Several hundred absorption images were averaged to produce a final record of the fragment positions. To remove imaging artefacts and incidental absorption from unwanted atoms, the experimental sequence was alternated so that every other image contained none of the desired fragments, but everything else. The final image was then computed as the averaged difference between these interlaced 'with fragment' and 'without fragment' images. For Fig. 2 insets and side-view data, we also used an optical pulse to deplete the ground-state population with $J=2$ before photodissociating the $J_i=0$ states.

Forbidden photodissociation angular distributions. A comparison of experimental images of fragment distributions and calculations for the M1/E2 photodissociation of Fig. 3 is presented in Extended Data Fig. 1. Note that a large light intensity was required to drive the forbidden photodissociation process sufficiently rapidly to observe these angular distributions. Besides power broadening the line shapes in Fig. 3b, this high intensity may have affected the measured fragment distributions in Extended Data Fig. 1.

Quasiclassical model. In the photodissociation literature there is a well-known quasiclassical model describing the angular distribution of fragments produced by the photodissociation of aligned molecules

$$I_{qc}(\theta,\phi) = |\Phi_i(\theta,\phi)|^2[1+\beta_{20}P_2^0(\cos\chi)] \quad (3)$$

where the angles are defined in the main text. For homonuclear diatomic molecules in the Born–Oppenheimer approximation, the probability density for the internuclear axis orientation of an initial state with quantum numbers J_i, M_i and $|\Omega_i|$ is given by Wigner–D functions as

$$|\Phi_i(\theta,\phi=0)|^2 = \frac{(2J_i+1)}{8\pi}(|D^{J_i}_{M_i\Omega_i}(0,\theta,0)|^2 + |D^{J_i}_{M_i,-\Omega_i}(0,\theta,0)|^2) \quad (4)$$

where Ω is the internuclear projection of the electronic angular momentum.

We observe disagreement with the quasiclassical model in the majority of cases. At first glance this is surprising because, theoretically, the quasiclassical model has been shown to be either equivalent or a good approximation to the quantum mechanical result for most cases of one-photon E1 photodissociation of a diatomic molecule with prompt axial recoil[19]. However, our measurements are performed at very low continuum energies to reach the ultracold chemistry regime, and thus may violate the assumption of axial recoil[5]. Additionally, ref. 19 predicted that the quasiclassical model should fail for the special case of 'perpendicular' transitions ($|\Delta\Omega|=1$) with initial states that are a superposition of Ω_i states differing by ±2. This special case includes our measurements of 1_u initial states in Fig. 4, and our observations support this prediction.

Extended Data Fig. 2 compares the quasiclassical model with both quantum mechanical predictions and experimental images for several cases. For each, the construction of the quasiclassical prediction is outlined. As in Fig. 4, we use coloured dots to indicate the level of agreement between the two predictions. To determine this agreement, the quasiclassical model neglected the nonadiabatic Coriolis mixing of $|\Omega_i|$ (ref. 32). There is also some ambiguity in choosing a value of β_{20} to use with the quasiclassical model. Conventionally, β_{20} should be equal to 2 for parallel transitions with $\Delta\Omega=0$ and to −1 for perpendicular transitions with $|\Delta\Omega|=1$. In cases of persistent disagreement, we varied β_{20} as a free parameter within the physically allowed range of [−2, 1]. Such a variation has been considered previously as an effect of the breakdown of the axial-recoil approximation[34].

We do observe three cases of exact agreement (indicated by green dots in Extended Data Fig. 3), two of which are highlighted in Extended Data Fig. 2. The reason the quasiclassical model gives exact results is that selection rules only allow a single J in these cases, making the axial-recoil approximation no longer necessary. Specifically, these cases correspond to 0_u^+ initial states with odd J_i for either $|M_i|=J_i$ with $p=0$ or $J_i=1$ and $M_i=0$ with $|p|=1$, for which the angular distribution is energy independent. Agreement occurred here without needing to adjust β_{20}.

In Fig. 2, $p=0$ and the initial state $J_i=M_i=0$ is spherically symmetric, so the angular distribution is parameterized only by β_{20}. Thus, the quasiclassical model can always be adjusted to agree at any continuum energy.

Photodissociation of 0_u^+ states. Single-photon E1 photodissociation of 0_u^+ excited states to the ground continuum is shown in Extended Data Fig. 3, in analogy with Fig. 4 for 1_u states. In Fig. 4 and Extended Data Figs 2–4, the sign of M_i does not affect the results, and our experiments used $M_i>0$ for some of the data sets and $M_i<0$ for others. To avoid confusion we did not label the figures with $|M_i|$, which suggests a superposition of M_i, but instead chose M_i to be positive in the figures.

Spontaneous photodissociation. Extended Data Fig. 4a contains images of the fragments following spontaneous decay of the excited state $0_u^+(v_i=-3, J_i=3, M_i)$ to the ground continuum. As we selectively populate individual M_i sublevels, the measured distributions are anisotropic. They are well described by the incoherent superposition

$$I(\theta) \approx \sum_M |Y_{4M}(\theta,\phi=0)|^2 \begin{pmatrix} 4 & 1 & 3 \\ -M & M-M_i & M_i \end{pmatrix}^2 \quad (5)$$

Here, J is restricted to 4 because the strongest decay is to the $J=4$ shape resonance in the ground continuum. If all M_i were equally populated, which would add a sum over M_i to equation (5), then the distribution would be isotropic.

The shape resonance aids the measurement of the angular distributions because it favours a narrow range of continuum energies. Extended Data Figure 4b contains the results of pBasex analysis of the inset image and highlights how the radial distribution of the atomic fragments is clustered around 66 MHz, revealing an ~10 ns shape resonance lifetime. Extended Data Figure 4c shows that the angular distribution from this analysis matches expectations from equation (5).

Absorption images in figures. Supplementary Tables 1–3 list the parameters used to generate the theoretical images shown in Fig. 4 and Extended Data Figs 1–3. To display theoretical results as simulated absorption images, the intensities are projected into the yz plane by integrating over the x direction. To approximate the blurring present in experimental images from limited optical resolution and light pulse durations, the image is convolved with a Gaussian distribution

$$N(y,z) \propto \int_{-\infty}^{\infty} e^{-\left(\sqrt{x^2+y^2+z^2}-R_0\right)^2/(2\sigma^2)} I(\theta,\phi)\,dx \quad (6)$$

where R_0 is the mean radius, σ is the standard deviation, $\theta=\cos^{-1}\left(z/\sqrt{x^2+y^2+z^2}\right)$ and $\phi=\sin^{-1}\left(y/\sqrt{x^2+y^2}\right)$. The fractional blur was $\sigma/R_0=0.05$ except for Extended Data Fig. 4, where $\sigma/R_0=0.2$.

The same colouring scheme (Matlab colourmap jet) is used in all experimental and theoretical absorption images, up to differences between CMYK and RGB colour mode presentation. Each image was linearly rescaled to fit the finite range [0, 1] of this scheme. To ensure that the same colour corresponds to zero absorption in all images, despite the presence of noise and imaging artefacts, the experimental images are scaled to have an average value of 0.25 in zero-absorption regions and a maximum value of 1. Likewise, the theoretical images are scaled to have

a minimum value of 0.25 but a maximum value of 0.85 instead of 1, to be more visually similar to experimental images.

The field of view differs between experimental images because of cropping for presentation, and falls in the range of 0.1–0.9 mm on each side. For a given image, the field of view may be accurately determined by calculating the maximum diameter D of the photodissociation products as $D = C\tau\sqrt{(\varepsilon - U)/h}$. Here, the kinetic expansion time τ was 0.3 ms for Fig. 1, 0.8 ms for Fig. 2, 0.6 ms for Fig. 3, 0.3–0.4 ms for Fig. 4, 0.39 ms for Fig. 5, 0.6 ms for Extended Data Fig. 1, 0.3–0.4 ms for Extended Data Fig. 3 and 0.1 ms for Extended Data Fig. 4. The dissociation energies ε not labelled in insets are listed in Supplementary Tables 1–3. From conservation of energy, the parameter $C = 2.\sqrt{h/m_{Sr}} \approx 1.348 \times 10^{-4}$ ms$^{-1/2}$ and the lattice depth U must be included as a small offset[17,35]. For Fig. 1b, for example, this gives $D = 0.34$ mm. For theoretical images, D was set to 80% of the image width.

Extracting angular distribution parameters. For angular distributions that are cylindrically symmetric (depend only on θ), the polar basis set expansion (pBasex) algorithm[16] can extract the 3D distribution from 2D projections such as absorption images by fitting the data with the Abel transform of a weighted sum of the Legendre polynomials. We used the software implementation of the pBasex algorithm in ref. 36 to analyse the images in Figs 2 and 5 and Extended Data Fig. 4. For low signal-to-noise images, we found that the extracted distribution is artificially skewed towards spherical symmetry[35]. To eliminate this systematic error, we performed pBasex inversion on a background image made from the set of without-fragment images that is processed to remove imaging artefacts and rescaled so that the average value equals that of the background regions in the final image. The final distribution is then the difference between those extracted for the original image and for the background image. The parameters β_{20} of Fig. 2 and R and δ of Fig. 5 were determined from least-squares fitting of the number of fragments versus θ in the final distribution.

In some cases, such as with the $\varepsilon/h = 32$ MHz inset of Fig. 5b, experimental issues may lead to images with deviations from the expected cylindrical symmetry. This may occur, for example, from imperfect control of the photodissociating light polarization, which may introduce a 'skewness' in the distribution. Apparent deviations from perfect cylindrical symmetry may also have occurred because of absorption imaging error induced by imperfectly correcting for the atomic saturation, which is especially important when the imaging beam exhibits substantial variations across its spatial profile (as was the case for our experiment). In such cases, we proceeded with pBasex analysis but included an estimate of the resulting bias when determining error bars.

For Fig. 2, further analysis was performed by integrating 2D projections along y to convert the images to 1D curves along z. This allows parameters such as β_{20} to be directly extracted by fitting the 1D curve with the expected angular distribution, similar to Extended Data Fig. 4c. Although this analysis can be performed with the axial-view images, for Fig. 2 we did this through separate experiments with images taken along the y axis, which had the benefits of a reduced optical depth and a smoother intensity profile of the imaging beam. These side-view images are 2D projections of the photofragment position onto the xz plane, and are complicated by the distribution of occupied sites in the optical lattice.

Calculation and parameterization of angular distributions. Supplementary Information details the calculation and parameterization of photodissociation angular distributions used in this work. Supplementary Tables 1–3 list the parameters for all of the theoretical images as well as experimental continuum energies.

31. Reinaudi, G., Osborn, C. B., McDonald, M., Kotochigova, S. & Zelevinsky, T. Optical production of stable ultracold $^{88}Sr_2$ molecules. *Phys. Rev. Lett.* **109,** 115303 (2012).
32. McGuyer, B. H. *et al.* Nonadiabatic effects in ultracold molecules via anomalous linear and quadratic Zeeman shifts. *Phys. Rev. Lett.* **111,** 243003 (2013).
33. Reinaudi, G., Lahaye, T., Wang, Z. & Guéry-Odelin, D. Strong saturation absorption imaging of dense clouds of ultracold atoms. *Opt. Lett.* **32,** 3143–3145 (2007).
34. Wrede, E., Wouters, E. R., Beckert, M., Dixon, R. N. & Ashfold, M. N. R. Quasiclassical and quantum mechanical modeling of the breakdown of the axial recoil approximation observed in the near threshold photolysis of IBr and Br_2. *J. Chem. Phys.* **116,** 6064–6071 (2002).
35. Apfelbeck, F. *Photodissociation Dynamics of Ultracold Strontium Dimers*. MSc thesis, Ludwig Maximilian University of Munich (2015).
36. O'Keeffe, P. *et al.* A photoelectron velocity map imaging spectrometer for experiments combining synchrotron and laser radiations. *Rev. Sci. Instrum.* **82,** 033109 (2011).

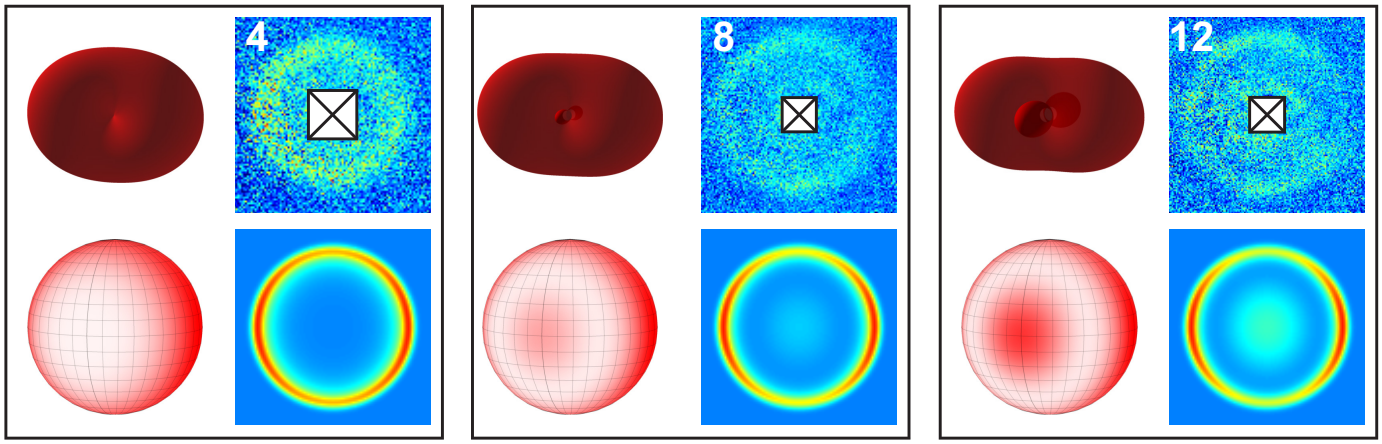

Extended Data Figure 1 | Angular distributions for the M1/E2 photodissociation of $1_g(v_i = -1, J_i = 1, M_i = 0)$ state with $p = 0$ to the ground continuum. Images are arranged as in Fig. 4. The experimental images are labelled by the continuum energy ε/h in MHz. To improve contrast, the strong centre dot from spontaneous decay, as seen in Fig. 3b, was removed before processing and is covered by a box. The theoretical images are calculated using a quantum chemistry model.

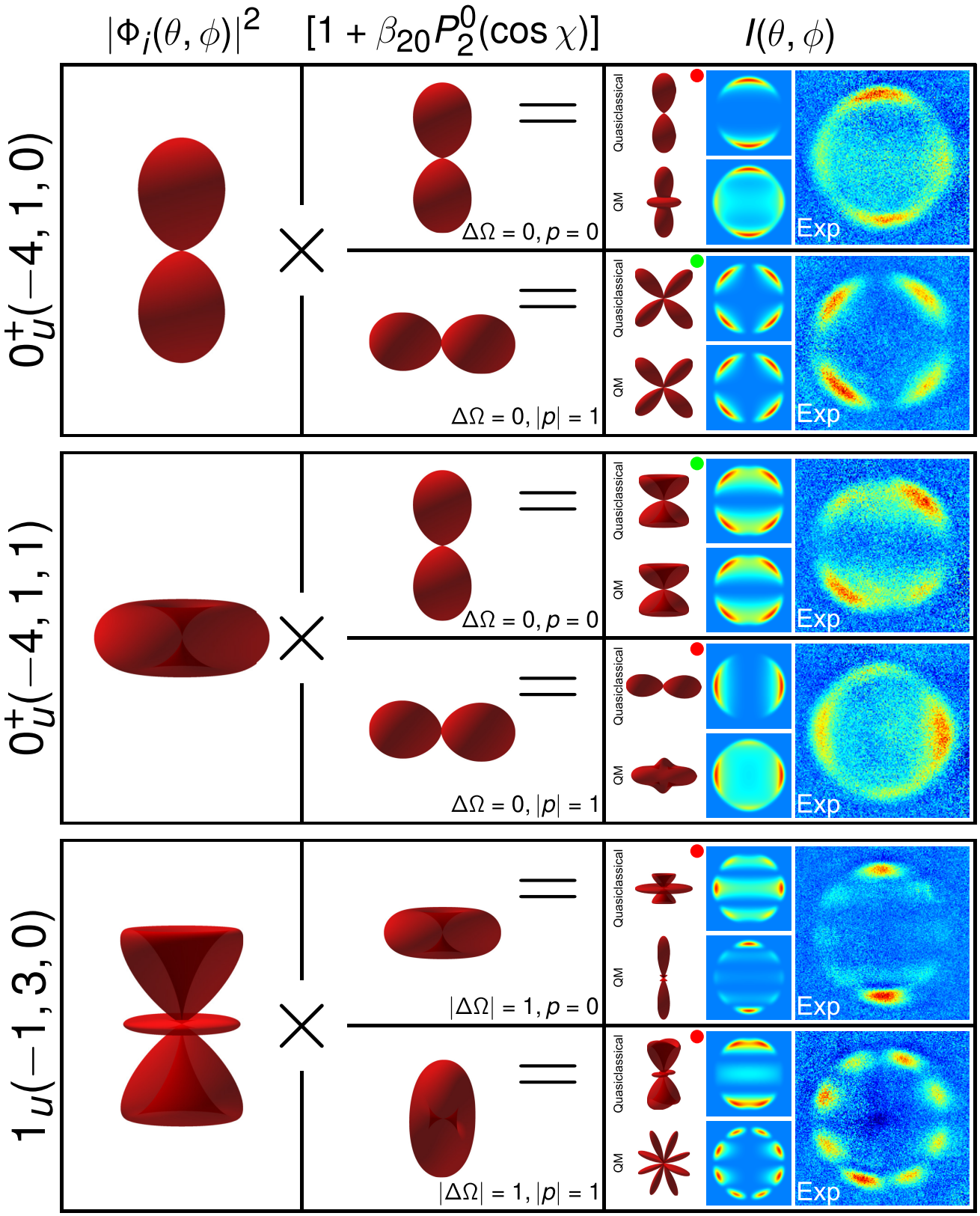

Extended Data Figure 2 | Comparison of quasiclassical and quantum mechanical (QM) theory with experimental (Exp) images for selected cases from Fig. 4 and Extended Data Fig. 3. The quasiclassical predictions follow from equations (3) and (4) assuming $\beta_{20}=2$ for $\Delta\Omega=0$ and -1 for $|\Delta\Omega|=1$. (The quantum mechanical predictions slightly differ from those displayed in Fig. 4 and Extended Data Fig. 3 because they are the full quantum mechanical calculations given in Supplementary Tables 2 and 3.) As before, coloured dots indicate the level of quasiclassical agreement.

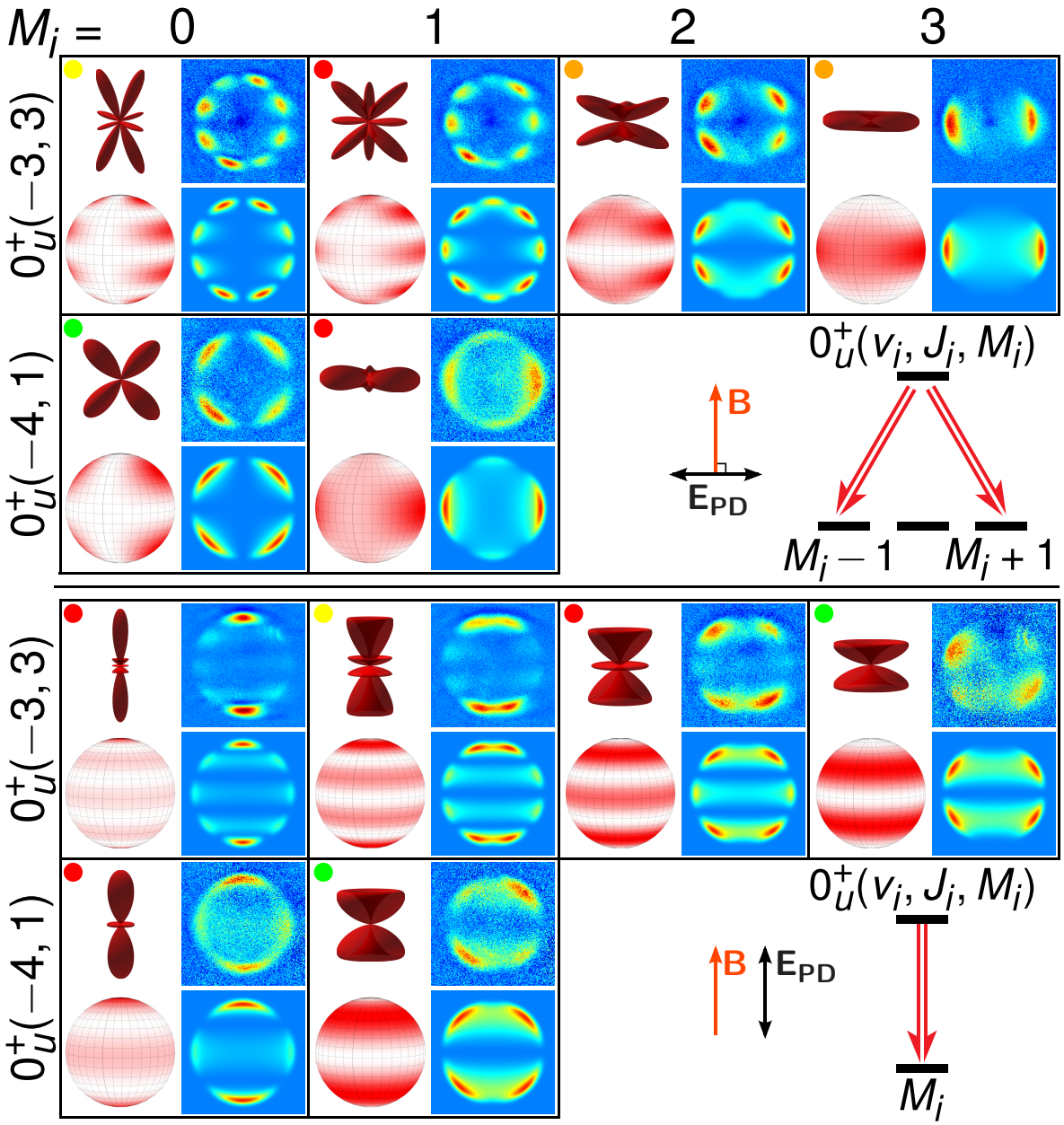

Extended Data Figure 3 | Photodissociation of molecules near the $^1S + {}^3P_1$ threshold to the ground-state continuum. In contrast to Fig. 4, here the initial states are 0_u^+ with $(v_i, J_i) = (-4, 1)$ or $(-3, 3)$ as indicated. These initial states lead to nearly identical distributions as those with the 1_u initial states, contrary to the quasiclassical picture. As before, compatibility with the quasiclassical approximation is indicated by the coloured dots.

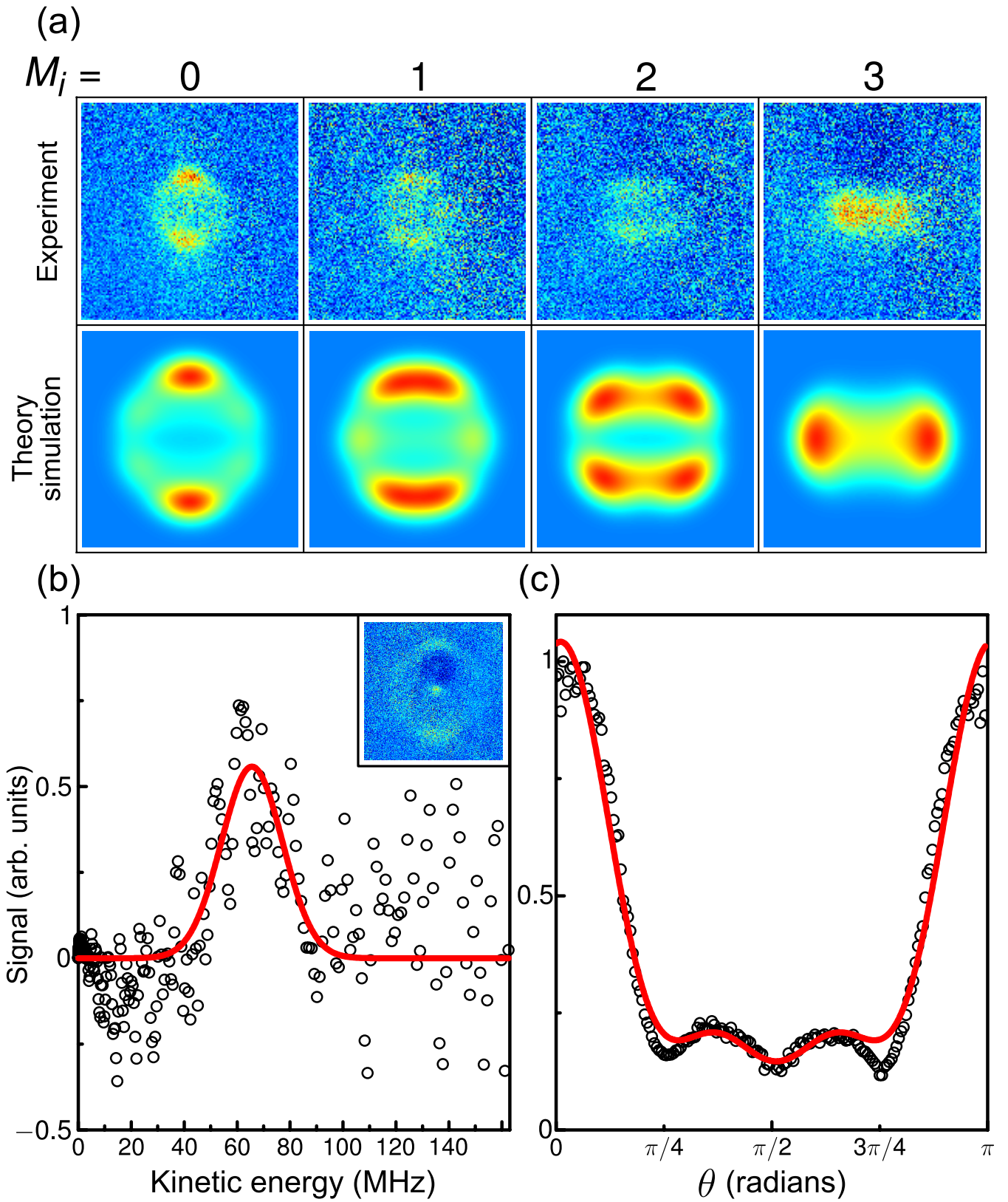

Extended Data Figure 4 | Spontaneous photodissociation of molecules prepared in $0_u^+(v_i = -3, J_i = 3, M_i)$ states. a, Absorption images of angular distributions versus M_i. Theoretical simulations using equation (5) are shown underneath. A short expansion time was used to increase visibility. **b**, For quantitative analysis, another image (inset) of the $M_i = 0$ case was taken with a longer expansion time and analysed with the pBasex algorithm. The extracted fragment radial distribution shows a focusing around a certain kinetic energy, which was determined by fitting with a Gaussian (red curve). Correcting for an offset due to the lattice depth[35], this energy corresponds to a shape resonance with a binding energy of -66 ± 3 MHz. **c**, The extracted fragment angular distribution qualitatively matches the calculation (red curve) of equation (5).

SUPPLEMENTARY INFORMATION

doi:10.1038/nature18314

Photodissociation of ultracold diatomic strontium molecules with quantum state control

M. McDonald,[1] B. H. McGuyer,[1] F. Apfelbeck,[1*] C.-H. Lee,[1]
I. Majewska,[2] R. Moszynski,[2] T. Zelevinsky[1†]

[1]Department of Physics, Columbia University, 538 West 120th Street, New York, NY 10027-5255, USA
[2]Quantum Chemistry Laboratory, Department of Chemistry, University of Warsaw,
Pasteura 1, 02-093 Warsaw, Poland
[*]Present address: Faculty of Physics, Ludwig Maximilian University of Munich,
Schellingstrasse 4, 80799 Munich, Germany
[†]To whom correspondence should be addressed; E-mail: tz@phys.columbia.edu.

Contents

1 Supplementary Methods

1.1 Parametrizing angular distributions

1.1.1 Anisotropy (or beta) parameters

We can represent the angular distribution of any physical intensity (or differential cross section) with the expansion

$$I(\theta,\phi) \propto 1 + \sum_{l=1}^{\infty} \sum_{m=0}^{l} P_l^m(\cos\theta)\Big[\beta_{lm}\cos(m\phi) + \gamma_{lm}\sin(m\phi)\Big] \tag{7}$$

in terms of real-valued "anisotropy" coefficients β_{lm} and γ_{lm}, where $\gamma_{l0} \equiv 0$. If there is no dependence on ϕ the associated Legendre polynomials reduce to Legendre polynomials, $P_l^0(\cos\theta) = P_l(\cos\theta)$, and the remaining coefficients β_{l0} are conventionally denoted β_l.

If both atomic fragments of a dissociated homonuclear diatomic molecule are detected equally, then conservation of momentum requires the inversion symmetry $I(\pi-\theta,\phi+\pi)=I(\theta,\phi)$. The expansion (7) has this symmetry if the coefficients with odd l are zero.

If the only nonzero coefficients are those with even $l+m$, then the expansion (7) will additionally be symmetric under reflection across the equator, $I(\pi-\theta,\phi)=I(\theta,\phi)$. For homonuclear diatomic molecules, this symmetry requires the coefficients with odd m to be zero. Intensities without this symmetry display a "skewness," such as the asymmetry in Fig. 1(b) and several other figure insets that are likely due to imperfect laser polarization or incomplete saturation correction during absorption imaging.

1.1.2 Partial scattering amplitudes

For our experiments, the measured intensity (or differential cross section) can be written as a sum of the squared absolute values of complex scattering amplitudes for separate electronic channels,

$$I(\theta,\phi)=\sum_{\Omega}\left|f^{\{\Omega\}}(\theta,\phi)\right|^2, \tag{8}$$

here indexed by the quantum number Ω for the internuclear projection of angular momentum.

To calculate the intensity, we compute the partial scattering amplitudes $f_{JM}^{\{\Omega\}}$ of a partial-wave expansion of the scattering amplitude in terms of angular basis functions,

$$f^{\{\Omega\}}(\theta,\phi)=\sum_{JM} f_{JM}^{\{\Omega\}}\,\psi_{JM}^{\{\Omega\}}(\theta,\phi), \tag{9}$$

as described in Sec. 1.2.1. In terms of Wigner D-functions, we chose the angular basis functions to be

$$\psi_{JM}^{\{\Omega\}}(\theta,\phi)=\sqrt{\frac{2J+1}{4\pi}}\,D^{J*}_{M\Omega}(\phi,\theta,0), \tag{10}$$

so that for $\Omega=0$ they are equivalent to spherical harmonics, $\psi_{JM}^{\{0\}}(\theta,\phi)=Y_{JM}(\theta,\phi)$.

The expansion (7) is equivalent to Eq. (8) if we write the anisotropy coefficients as the real and imaginary parts of a weighted sum over products of pairs of partial scattering amplitudes,

$$\beta_{lm}+i\gamma_{lm}=\sum_{\Omega,J,J',M} W_{lm}(\Omega,J,J',M)\; f_{JM}^{\{\Omega\}*}\, f_{J',M-m}^{\{\Omega\}}\Big/\sum_{JM\Omega}\left|f_{JM}^{\{\Omega\}}\right|^2. \tag{11}$$

The real-valued weights may be written in terms of Wigner 3j symbols as

$$W_{lm}(\Omega,J,J',M)=(-1)^{M-\Omega}\frac{2[l]}{1+\delta_{m0}}\sqrt{\frac{[J][J'](l-m)!}{(l+m)!}}\begin{pmatrix}J' & l & J\\ m-M & -m & M\end{pmatrix}\begin{pmatrix}J' & l & J\\ -\Omega & 0 & \Omega\end{pmatrix}, \tag{12}$$

where the shorthand $[J]\equiv 2J+1$ and δ_{ij} is a Kronecker delta. As an aside, note that the quantities $\rho^{\{\Omega JJ'\}}_{M,M-m}=f_{JM}^{\{\Omega\}*}\,f_{J',M-m}^{\{\Omega\}}/\sum_{JM\Omega}\left|f_{JM}^{\{\Omega\}}\right|^2$ in Eq. (11) have properties similar to density matrix elements.

From these weights W_{lm} and the properties of 3j symbols, the maximum value of l contributing in the expansion (7) is limited to twice the largest value of J for which there is a nonzero $f_{JM}^{\{\Omega\}}$. The maximum value of m is limited by the furthest off-diagonal magnetic coherence, that is, the nonzero quantity $f_{JM}^{\{\Omega\}*}\,f_{J',M-m}^{\{\Omega\}}$ with largest $m=M-M'$.

1.2 Calculation of angular distributions

1.2.1 Theoretical description of photodissociation

The theory of photodissociation employed here follows the seminal work of Ref. [1]. The fragmentation process is characterized by the differential cross section that is defined by Fermi's golden rule with the

electric-dipole (E1), magnetic-dipole (M1), or electric-quadrupole (E2) transition operators. Since we work with a coupled manifold of electronic states for both the ungerade bound states and ungerade continuum, we do not assume the Born-Oppenheimer approximation in contrast to Zare [1]. In this case the theory of photodissociation for diatomic molecules is very similar to the non-degenerate atom-diatom case treated in detail by Balint-Kurti and Shapiro [2, 3].

In the absence of external fields, the wave function of the initial (bound) state depends on the set of the electronic coordinates $\{\mathbf{r}\}$ and on the vector $\mathbf{R} = (R, \Theta, \Phi)$ describing the relative motion of the nuclei, and is given by

$$\Psi^{p_i}_{J_i M_i}(\{\mathbf{r}\}, \mathbf{R}) = \sum_{\Omega_i=-J_i}^{J_i} \sqrt{\frac{2J_i+1}{16\pi^2(1+\delta_{\Omega_i 0})}} \left(D^{J_i\star}_{M_i\Omega_i}(\Phi,\Theta,0)\psi^{p_i}_{J_i\Omega_i}(\{\mathbf{r}\},R) + \sigma_i D^{J_i\star}_{M_i,-\Omega_i}(\Phi,\Theta,0)\psi^{p_i}_{J_i,-\Omega_i}(\{\mathbf{r}\},R)\right), \quad (13)$$

where $\sigma_i = p_i(-1)^{J_i}$ is the spectroscopic parity and J_i, M_i, and p_i are the quantum numbers of the total angular momentum, its projection on the space-fixed Z axis (previously denoted z), and the parity with respect to space-fixed inversion. Note that in the above expression the quantum number π_i related to the action of the reflection in the body-fixed yz plane on the electronic coordinates does not appear. In our case it is equal to zero, and the parity of the $\Omega_i = 0$ electronic states is always "+".

In Hund's case (c) the internal wave function $\psi^{p_i}_{J_i\Omega_i}(\{\mathbf{r}\}, R)$ can be represented by the Born-Huang expansion [4, 5]

$$\psi^{p_i}_{J_i\Omega_i}(\{\mathbf{r}\}, R) = \sum_n \phi_{n,\Omega_i}(\{\mathbf{r}\}; R)\chi^{p_i}_{nJ_i\Omega_i}(R). \quad (14)$$

Here, the $\phi_{n,\Omega_i}(\{\mathbf{r}\}; R)$ are electronic wave functions, that is, the solutions of the electronic Schrödinger equation including spin-orbit coupling, which depend parametrically on the interatomic distance R. The $\chi^{p_i}_{nJ_i\Omega_i}(R)$ are rovibrational wave functions. Finally, the index n labels all relativistic dissociation channels. Note that for homonuclear diatomic molecules the electronic wave function has an additional gerade/ungerade (g/u) symmetry resulting from the $D_{\infty h}$ point group of the molecule. For simplicity we do not indicate the g/u symmetry in the notation $\phi_{n,\Omega_i}(\{\mathbf{r}\}; R)$. The rovibrational wave functions are solution of a system of coupled differential equations. See, for instance, Ref. [6] for the equations corresponding to the ungerade excited manifold of the electronic states.

The wave function $\Psi^{p_f}_{\mathbf{k}}(\{\mathbf{r}\}, \mathbf{R})$ of the final continuum state corresponding to the wave vector $\mathbf{k} = (k, \theta, \phi)$ can be represented by the following expansion reflecting different partial waves J of the fragmented atoms,

$$\Psi^{p_f}_{\mathbf{k}}(\{\mathbf{r}\}, \mathbf{R}) = \sum_{JM} \sum_{\Omega=-J}^{J} \sum_{\Omega'=-J}^{J} \frac{(2J+1)}{4\pi\sqrt{2\pi(1+\delta_{\Omega' 0})}} \mathcal{C}^{jp}_{m_j\Omega} D^{J}_{M\Omega}(\phi,\theta,0) D^{J*}_{m_J\Omega}(\phi,\theta,0) \times \left(D^{J\star}_{M\Omega'}(\Phi,\Theta,0)\psi^{Jp_f}_{\Omega'\Omega}(\{\mathbf{r}\},R) + \sigma_i D^{J\star}_{M,-\Omega'}(\Phi,\Theta,0)\psi^{Jp_f}_{-\Omega',\Omega}(\{\mathbf{r}\},R)\right), \quad (15)$$

where j denotes the total angular momentum of the photofragmented atoms, m_j is its projection in the space-fixed Z axis, and p is the product of atomic parities. The numerical coefficients $\mathcal{C}^{jp}_{m_j\Omega}$ depend on the states of the photofragmented atoms and can be found in Ref. [7]. The internal wave function is given by the following multichannel generalization of the Born-Huang expansion,

$$\psi^{Jp_i}_{\Omega'\Omega}(\{\mathbf{r}\}, R) = \sum_n \phi_{n,\Omega'}(\{\mathbf{r}\}; R)\chi^{Jp_f}_{n\Omega'\Omega}(R), \quad (16)$$

where $\chi^{Jp_f}_{n\Omega'\Omega}(R)$ is a radial channel function that satisfies the boundary condition

$$\chi^{Jp_f}_{n\Omega'\Omega}(R) \approx R\sqrt{\frac{2\mu k}{\pi}} \left(\delta_{\Omega'\Omega} j_J(kR) + S^{Jp_f}_{n\Omega'\Omega} n_J(kR)\right) \quad (\text{for } R \longrightarrow \infty) \quad (17)$$

in terms of the scattering matrix $S^{Jp_f}_{n\Omega'\Omega}$. Here, μ is the reduced mass and j_J, n_J are spherical Bessel functions.

In this work we considered four different photofragmentation processes: (i) the E1 process starting from the ungerade manifold of the electronic states that correspond to the $^1S + {}^3P_1$ dissociation limit and ending at the ground electronic continuum, (ii) the M1 and (iii) the E2 processes starting from the gerade manifold corresponding to the same dissociation limit and ending at the ground electronic continuum, and finally (iv) the E1 process starting from ground state molecules and ending at the ungerade manifold corresponding to the $^1S + {}^3P_1$ dissociation limit.

The first three processes begin with manifolds that are described by two coupled electronic states: 0^+_u and 1_u for the E1 process and 0^+_g and 1_g for the M1 and E2 processes. The corresponding wave functions for the initial states are given by Eqs. (13) and (14) with the summation over Ω_i limited to -1, 0, and 1, and with n fixed to $^1S + {}^3P_1$. The wave function for the final continuum state, however, corresponds to the Born-Oppenheimer approximation and is given by Eqs. (15) and (14) with only the $\Omega = 0$ term and with n fixed to $^1S + {}^1S$. Note that in the single-channel approximation $\Omega = \Omega'$, so for simplicity we denote the rovibrational wavefunction by $\chi^{Jp_f}_{n\Omega}(R)$. The electronic transition operator for the E1 process was assumed to be constant and proportional to the atomic value, while the operators for the M1 and E2 transitions followed the asymptotic form of Refs. [8, 9]. Otherwise, the remaining derivation of the expression for the differential cross section follows Ref. [1] and is not reproduced here, although the multichannel character of the initial state wave functions complicates the angular momentum algebra.

Now we discuss the boundary condition for the final continuum rovibrational wave function $\chi^{Jp_f}_{n\Omega}(R)$. The single-channel approximation is valid for the 0^+_g ground electronic continuum. In this case, at large internuclear distances R the partial wave expansion (15) becomes [10]

$$\chi^{Jp_f}_{n\Omega}(R) \approx i^J e^{i\delta_J} \sqrt{\frac{2\mu}{\pi\hbar^2 k}} \sin(kR + \delta_J + J\pi) \quad (\text{for } R \longrightarrow \infty), \tag{18}$$

where δ_J is the phase shift for a given partial wave J. However, in practice it is more convenient to work with real functions than with complex functions that satisfy this boundary condition. Therefore, we chose to instead use the real-valued large-R boundary condition [10]

$$\chi^{Jp_f}_{n\Omega}(R) \approx \sqrt{\frac{2\mu}{\pi\hbar^2 k}} \sin(kR + \delta_J + J\pi) \quad (\text{for } R \longrightarrow \infty), \tag{19}$$

and to include the phase factor $i^J e^{i\delta_J}$ in the partial scattering amplitudes.

Therefore, for the first three processes the differential cross section is given by Eq. (8) with $\Omega = 0$. The partial scattering amplitudes in the expansion (9) for this scattering amplitude are then given by

$$f^{\{\Omega\}}_{JM} = \sum_{\Omega_i=-J_i}^{J_i} 2i^J e^{i\delta_J} \sqrt{\frac{4\pi(2J_i+1)}{(1+\delta_{\Omega_i 0})(1+\delta_{\Omega 0})}} \langle \chi^{p_f}_{nkJ\Omega} | T^L_{\Omega-\Omega_i} | \chi^{p_i}_{nJ_i\Omega_i} \rangle \begin{pmatrix} J & L & J_i \\ -\Omega & \Omega-\Omega_i & \Omega_i \end{pmatrix} \begin{pmatrix} J & L & J_i \\ -M & M-M_i & M_i \end{pmatrix}, \tag{20}$$

where $T^L_{\Omega-\Omega_i}$ is the electronic transition operator of rank $L = 1$ for E1 or M1 transitions and $L = 2$ for E2 transitions for the experimental conditions described in Sec. 1.2.2. The anisotropy parameters in the expansion (7) then follow from using these partial amplitudes with Eqs. (11) and (12).

The M1 and E2 processes were not observed separately because of selection rules. In this case, both processes must be included and the observed cross section may be written as the sum

$$I(\theta, \phi) = \left| f^{\{0\}}_{JM,\text{M1}} + f^{\{0\}}_{JM,\text{E2}} \right|^2, \tag{21}$$

of separate scattering amplitudes (9) using Eq. (20). This expression explicitly allows for interference between the M1 and E2 processes. Note that this interference may affect the angular distribution even if it does not affect the strength of the transition, which is proportional to the integral of the differential cross section over all angles. The strength curves in Fig. 3(b) were calculated this way, and were included in the figure

by scaling their amplitudes together to better match experiment, while keeping their relative amplitudes fixed by theory. Note that the experimental procedure used to produce the data in Fig. 3(b) is an imperfect measure of the photodissociation lineshape, so the comparison with theory is qualitative.

Finally, for the fourth process of photofragmentation beginning with ground state molecules and ending at the $^1S + {}^3P_1$ continuum, the wave function of the initial (bound) state satisfies the Born-Oppenheimer approximation. Therefore we set $\Omega_i = 0$ in Eq. (13) and limit the Born-Huang expansion (14) to a single product. However, the partial wave expansion (15) for the final continuum must explicitly account for the Coriolis coupling between the 0_u^+ and 1_u electronic states, and for the angular momentum $j = 1$ and total parity $p = -1$ of the atomic fragments. For this multichannel continuum case, we imposed the complex boundary conditions of Eq. (17). The remaining derivation of the expression for the differential cross section follows Refs. [11, 2, 3, 12]. The differential cross section $I(\theta, \phi)$ then follows from Eqs. (8) and (9) using the partial scattering amplitudes

$$f_{JM}^{\{\Omega\}} = \sum_{\Omega_i=-J_i}^{J_i} \sum_{\Omega'=-J_i}^{J_i} 2\sqrt{\frac{4\pi(2J_i+1)}{(1+\delta_{\Omega_i 0})(1+\delta_{\Omega' 0})}} \langle \chi_{n\Omega'\Omega}^{J p_f} | T^L_{\Omega'-\Omega_i} | \chi_{nJ_i\Omega_i}^{p_i} \rangle \begin{pmatrix} J & j & J_i \\ -\Omega' & \Omega'-\Omega_i & \Omega_i \end{pmatrix} \begin{pmatrix} J & j & J_i \\ -M & M-M_i & M_i \end{pmatrix}. \tag{22}$$

1.2.2 Field components for the experimental conditions

For E1 transitions in our experiment, the lab-frame spherical tensor components of the field driving the transition are

$$T^1_0(\mathbf{E}) = E_z \tag{23}$$

$$T^1_{\pm 1}(\mathbf{E}) = -\frac{i}{\sqrt{2}} E_y, \tag{24}$$

using the notation of Ref. [13]. For linear polarization parallel to the z axis, which is labeled "$p = 0$" in Fig. 4, $E_y = 0$. For linear polarization along the y axis, which is labeled "$|p| = 1$" in Fig. 4, $E_z = 0$. Likewise, for M1 transitions these components are

$$T^1_0(\mathbf{B}) = B_z \tag{25}$$

$$T^1_{\pm 1}(\mathbf{B}) = -\frac{i}{\sqrt{2}} B_y. \tag{26}$$

Note that in Fig. 3 "$p = 0$" now corresponds to linear polarization along the y axis, such that $B_y = 0$, and "$|p| = 1$" to linear polarization parallel to the z axis, such that $B_z = 0$. For electric E2 transitions, these components are

$$T^2_0(\nabla\mathbf{E}) = 0 \tag{27}$$

$$T^2_{\pm 1}(\nabla\mathbf{E}) = \mp\frac{1}{2}(ikE_z) \tag{28}$$

$$T^2_{\pm 2}(\nabla\mathbf{E}) = \pm\frac{i}{2}(ikE_y) \tag{29}$$

for traveling-wave light propagating along the x axis with wavenumber k [14].

For θ and ϕ defined as in Fig. 1, these experimental conditions produce angular distributions that can be described only with β_{lm} coefficients in the expansion (7), leading to the simplified form of Eq. (2).

1.2.3 Energy independent angular distributions

For $^{88}Sr_2$ photodissociation, there are a few cases where the angular distributions are independent of the continuum energy. For E1 photodissociation to the ground continuum (where symmetry restricts J to even values) this occurs if J_i is even because $\Delta J = 0, \pm 1$. This also occurs with odd J_i for either $|M_i| = J_i$

with $p = 0$ or $J_i = 1$ and $M_i = 0$ with $|p| = 1$, because selection rules only allow a single value of J in the continuum. For M1/E2 photodissociation to the ground continuum from $J_i = 1$, $M_i = 0$, this occurs when the dissociation laser is linearly polarized along the z axis, because of ΔM selection rules. In these cases, the energy-dependent radial integrals in Eq. (20) are common to all partial scattering amplitudes, so the angular distributions are independent of the continuum energy. They are also relatively simple to calculate, because they reduce to evaluating geometrical factors.

1.2.4 Single-J approximation for angular distributions

In a similar fashion, Eqs. (20) and (22) can be used to explore what range of angular distributions may occur in an experiment by making simplifying assumptions about the radial integrals. For example, for E1 photodissociation to the ground continuum we could approximate the radial matrix elements in Eq. (20) to be nonzero only for a single J but multiple M, such that

$$f_{JM}^{\{\Omega\}} \propto T^L_{M-M_i}(\mathbf{E}) \begin{pmatrix} J & L & J_i \\ -M & M-M_i & M_i \end{pmatrix}, \tag{30}$$

where $T^L_{M-M_i}(\mathbf{E})$ are the lab-frame spherical tensor components of the dissociating field, as described in Sec. 1.2.2 for our experimental conditions. For a selected initial state, the calculation of the angular distribution simplifies to evaluating geometrical factors that depend only on the allowed quantum numbers.

In addition to energy-independent cases, this approximation works well for the energy-dependent data in Fig. 4 with odd J_i, because the continuum energies were chosen so that a single J was responsible for most of each angular distribution: $J = 4$ for $J_i = 3, 4$ and $J = 2$ for $J_i = 1, 2$. This approximation also explains some interesting properties that we observe. For example, the $(M_i = 0, |p| = 1)$ cases are identical except for a 90° rotation in ϕ, which corresponds to alternating the sign of the β_{l2} parameters with J_i. For $M_i \neq 0$, a qualitatively similar rotation often occurs. Finally, for $|p| = 1$ the cases of $|M_i| = J$ have the same coefficients as those of $p = 0$ for $|M_i| = J - 1$, since they produce the same single sublevels M in the continuum.

1.3 Parameters for theoretical images in figures

Supplementary Tables 1, 2, and 3 list the parameters used to generate the theoretical images shown in Fig. 4 and Extended Data Figs. 1–3.

2 Supplementary Tables

Supplementary Table 1: Parameters β_{lm} of the theoretical images in Extended Data Fig. 1 for the $p = 0$ case of M1/E2 photodissociation of $1_g(v_i = -1, J_i = 1, M_i = 0)$.

ε/h (MHz)	β_{20}	β_{22}	β_{40}	β_{42}	β_{44}
4	0.4178	−0.3599	0.1095	−0.01290	0.002280
8	0.2475	−0.3563	0.3077	−0.03626	0.006409
12	−0.06407	−0.2117	0.4362	−0.05140	0.009087

Supplementary Table 2: Parameters β_{lm} of the theoretical images in Fig. 4 and Extended Data Fig. 2 for E1 photodissociation of $1_u(v_i = -1, J_i, M_i)$. Values for odd J_i that depend on the continuum energy ε (given below in MHz) are rounded to four significant figures. However, the energies for odd J_i were chosen so that Eq. (30) with $J = J_i + 1$ is a good approximation. Fig. 4 uses the values from this approximation, which are given on a second line as fractions. Extended Data Fig. 2 uses the unapproximated values. For even J_i, the values are independent of the continuum energy. Where the transition is forbidden by symmetry ($p_i = M_i = 0$, even J_i), the experimental pattern is enabled by an applied magnetic field that admixes excited states [15] such that the parameters correspond to the approximation (30) with the substitution $J_i \longrightarrow J_i \pm 1$. Omitted values are zero because of symmetry.

J_i	$\lvert M_i\rvert$	ε/h	β_{20}	β_{22}	β_{40}	β_{42}	β_{60}	β_{62}	β_{80}	β_{82}
						$\lvert p\rvert = 1$				
4	0	76	85/77	25/77	729/1001	81/1001	−1/11	1/22	−392/143	7/143
4	1	74	1360/1463	450/1463	6561/19019	81/1729	2/209	0	6664/2717	−105/2717
4	2	71	65/154	45/176	−243/728	−81/2288	5/8	−9/176	−245/143	21/1144
4	3	68	−40/121	20/121	−243/1573	−162/1573	−170/121	4/121	1400/1573	−7/1573
4	4	—	−5/11	0	−243/143	0	17/11	0	−56/143	0
3	0	71	0.3097	−0.3909	0.3584	−0.05354	0.8934	−0.009862	−2.561	−0.04574
			85/77	−25/77	729/1001	−81/1001	−1/11	−1/22	−392/143	−7/143
3	1	71	0.1445	−0.2850	−0.1389	−0.01507	−1.653	−0.007708	1.816	0.03244
			400/539	−150/539	−1539/7007	−27/637	−10/11	0	280/143	5/143
3	2	72	−0.4966	−0.1545	−1.515	0.02140	1.633	0.03091	−0.6213	−0.01110
			−20/77	−15/88	−5589/4004	27/1144	59/44	3/88	−98/143	−7/572
3	3	72	−1.835	−0.05559	1.208	0.03464	−0.4569	−0.01112	0.08381	0.001497
			−3880/2233	−20/319	30861/29029	162/4147	−134/319	−4/319	392/4147	7/4147
2	0	52	5/7	5/14	−12/7	1/7				
2	1	48	2/7	2/7	12/7	−3/35				
2	2	44	5/7	0	−12/7	0				
1	0	32	5/7	−5/14	−12/7	−1/7				
1	1	31	−0.3445	−0.1311	0.1921	0.01601				
			−50/49	−10/49	36/49	3/49				
						$p = 0$				
4	0	77	100/77		1458/1001		20/11		490/143	
4	1	78	85/77		729/1001		−1/11		−392/143	
4	2	71	40/77		−81/91		−2		196/143	
4	3	68	−5/11		−243/143		17/11		−56/143	
4	4	—	−20/11		162/143		−4/11		7/143	
2	0	56	10/7		18/7					
2	1	55	5/7		−12/7					
2	2	44	−10/7		3/7					

Supplementary Table 3: Parameters β_{lm} of the theoretical images in Extended Data Fig. 2 and 3 for E1 photodissociation of $0_u^+(v_i, J_i, M_i)$, with $v_i = -3$ for $J_i = 3$ and $v_i = -4$ for $J_i = 1$. Only odd J_i are allowed by symmetry. The values that depend on the continuum energy ε (given below in MHz) are rounded to four significant figures. However, as in Supplementary Table 2, the energies were chosen so that Eq. (30) with $J = J_i + 1$ is a good approximation. Extended Data Fig. 3 uses these approximate values, which are given on a second line as fractions below. Extended Data Fig. 2 uses the unapproximated values. Omitted values are zero because of symmetry.

J_i	$\lvert M_i\rvert$	ε/h	β_{20}	β_{22}	β_{40}	β_{42}	β_{60}	β_{62}	β_{80}	β_{82}
						$\lvert p\rvert = 1$				
3	0	72	0.5258	−0.3728	0.4946	−0.05980	0.6317	−0.01999	−2.652	−0.04736
			85/77	−25/77	729/1001	−81/1001	−1/11	−1/22	−392/143	−7/143
3	1	71	0.3251	−0.2842	−0.2059	−0.02529	−1.437	−0.005318	1.893	0.03381
			400/539	−150/539	−1539/7007	−27/637	−10/11	0	280/143	5/143
3	2	70	−0.4253	−0.1640	−1.463	0.02271	1.548	0.03281	−0.6596	−0.01178
			−20/77	−15/88	−5589/4004	27/1144	59/44	3/88	−98/143	−7/572
3	3	69	−1.801	−0.06003	1.161	0.03740	−0.4509	−0.01201	0.09050	0.001616
			−3880/2233	−20/319	30861/29029	162/4147	−134/319	−4/319	392/4147	7/4147
1	0	33	5/7	−5/14	−12/7	−1/7				
1	1	32	−0.4751	−0.03716	0.3941	0.03284				
			−50/49	−10/49	36/49	3/49				
						$p = 0$				
3	0	72	2.131		2.272		3.022		3.223	
			100/77		1458/1001		20/11		490/143	
3	1	73	1.861		0.7914		−1.079		−2.573	
			85/77		729/1001		−1/11		−392/143	
3	2	74	0.9400		−1.677		−1.561		1.298	
			40/77		−81/91		−2		196/143	
3	3	75	−5/11		−243/143		17/11		−56/143	
1	0	33	0.4265		1.035					
			10/7		18/7					
1	1	32	5/7		−12/7					

Supplementary References

[1] R. N. Zare, "Photoejection Dynamics," Mol. Photochem. **4**, 1–37 (1972).

[2] G. G. Balint-Kurti and M. Shapiro, "Photofragmentation of triatomic molecules. Theory of angular and state distribution of product fragments," Chem. Phys. **61**, 137–155 (1981).

[3] G. G. Balint-Kurti and M. Shapiro, *Quantum Theory of Molecular Photodissociation*, in *Advances in Chemical Physics: Photodissociation and Photoionization*, Volume 60 (ed. K. P. Lawley), John Wiley & Sons, Inc., Hoboken, NJ, 1985.

[4] M. Born and K. Huang, *Dynamical Theory of Crystal Lattices*, Oxford University Press, Oxford, 1956.

[5] B. Bussery-Honvault, J.-M. Launay, T. Korona, and R. Moszynski, "Theoretical spectroscopy of the calcium dimer in the $A\ ^1\Sigma_u^+$, $c\ ^3\Pi_u$, and $a\ ^3\Pi_u^+$ manifolds: An *ab initio* nonadiabatic treatment," J. Chem. Phys. **125**, 114315 (2006).

[6] W. Skomorowski, F. Pawłowski, C. P. Koch, and R. Moszynski, "Rovibrational dynamics of the strontium molecule in the $A\ ^1\Sigma_u^+$, $c\ ^3\Pi_u$, and $a\ ^3\Sigma_u^+$ manifold from state-of-the-art *ab initio* calculations," J. Chem. Phys. **136**, 194306 (2012).

[7] D. V. Kupriayanov and O. S. Vasyutinskii, "Orientation and alignment of $^2P_{3/2}$ fragments following photodissociation of heteroatomic molecules," Chem. Phys. **171**, 25–44 (1993).

[8] B. Bussery-Honvault and R. Moszynski, "*Ab initio* potential energy curves, transition dipole moments and spinorbit coupling matrix elements for the first twenty states of the calcium dimer," Mol. Phys. **104**, 2387-2402 (2006).

[9] B. H. McGuyer, M. McDonald, G. Z. Iwata, M. G Tarallo, W. Skomorowski, R. Moszynski, and T. Zelevinsky, "Precise study of asymptotic physics with subradiant ultracold molecules," Nature Phys. **11**, 32–36 (2015).

[10] R. D. Levine, *Quantum Mechanics of Molecular Rate Processes*, Oxford University Press, Oxford, 1969, pp. 43–50.

[11] J. A. Beswick and R. N. Zare, "On the quantum and quasiclassical angular distributions of photofragments", J. Chem. Phys. **129**, 164315 (2008).

[12] P. S. Shternin and O. S. Vasyutinskii, "The parity-adapted basis set in the formulation of the photofragment angular momentum polarization problem: The role of the Coriolis interaction," J. Chem. Phys. **128**, 194314 (2008).

[13] J. R. Brown and A. Carrington, *Rotational Spectroscopty of Diatomic Molecules*, Cambridge University Press, Cambridge, 2003.

[14] M. Auzinsh, D. Budker, and S. Rochester. *Optically Polarized Atoms: Understanding light-atom interactions*, Oxford University Press, Oxford, 2010.

[15] B. H. McGuyer, M. McDonald, G. Z. Iwata, W. Skomorowski, R. Moszynski, and T. Zelevinsky, "Control of Optical Transitions with Magnetic Fields in Weakly Bound Molecules," Phys. Rev. Lett. **115**, 053001 (2015).